The Astrophysical Journal, 646:553–559, 2006 July 20

DIRECT MEASUREMENT OF TRAVEL-TIME KERNELS FOR HELIOSEISMOLOGY

T. L. Duvall, Jr.
Laboratory for Solar and Space Physics, NASA Goddard Space Flight Center, Greenbelt, MD 20771; thomas.l.duvall@nasa.gov
A. C. Birch
NorthWest Research Associates, Colorado Research Associates Division, Boulder, CO 80301; aaronb@cora.nwra.com
and
L. Gizon
Max-Planck-Institut für Sonnensystemforschung, 37191 Katlenburg-Lindau, Germany; gizon@mps.mpg.de
Received 2006 January 24; accepted 2006 March 30

ABSTRACT

Solar *f*-modes are surface gravity waves that propagate horizontally in a thin layer near the photosphere with a dispersion relation approximately that of deep water waves. At the power maximum near frequency $\omega/2\pi = 3$ mHz, the wavelength of 5 Mm is large enough for various wave scattering properties to be observable. Gizon & Birch have calculated spatial kernels for scattering in the Born approximation. In this paper, using isolated small magnetic features as approximate point scatterers, a linear-response kernel has been measured. In addition, the kernel has been estimated by deconvolving the magnetograms from the travel-time maps. The observed kernel is similar to the theoretical kernel for wave damping computed by Gizon & Birch: it includes elliptical and hyperbolic features. This is the first observational evidence to suggest that it is appropriate to use the Born approximation to compute kernels (as opposed to the ray approximation). Furthermore, the observed hyperbolic features confirm that it is important to take into account scattering of the waves coming from distant source locations (as opposed to the single-source approximation). The observed kernel is due to a superposition of the direct and indirect effects of the magnetic field. A simple model that includes both monopole and dipole scattering compares favorably with the data. This new technique appears to be promising to study how seismic waves interact with magnetic flux tubes.

Subject headings: methods: data analysis — scattering — Sun: helioseismology — Sun: magnetic fields — techniques: image processing

1. INTRODUCTION

In time-distance helioseismology (Duvall et al. 1993), travel times for waves between separated photospheric locations are measured. For a nonrotating Sun whose properties are only a function of radius, the travel times will be only a function of the distance between the photospheric locations. Inhomogeneities in the Sun will lead to local variations of the travel times. Time-distance helioseismology attempts to measure the travel-time variations and then to infer the solar inhomogeneities.

An important part of this process is the calculation of the forward problem, i.e., how the measured travel time depends on the inhomogeneities in the solar interior. Early work used ray theory to perform this computation (D'Silva & Duvall 1995; Kosovichev 1996). In the ray theory calculation, which is the limit of high frequency or infinite bandwidth, the travel-time variation only depends on the inhomogeneities along a single curve, or ray path, connecting the surface locations. Bogdan (1997) showed that finite-wavelength effects must be taken into account, so that the sensitivity to a perturbation extends beyond the ray path.

In more recent calculations (Birch & Kosovichev 2000; Gizon & Birch 2002; Birch et al. 2004), travel-time responses have been calculated as a single scattering off inhomogeneities using the Born approximation. In this paper, we consider *f*-modes that propagate horizontally in a thin layer close to the surface. An *f*-mode travel time can be measured from any surface location $\boldsymbol{r}_1$ to another location $\boldsymbol{r}_2$. Each pair of points $(\boldsymbol{r}_1, \boldsymbol{r}_2)$ is fully specified by the central location $\boldsymbol{r} = (\boldsymbol{r}_1 + \boldsymbol{r}_2)/2$ and the vector $\boldsymbol{\Delta} = \boldsymbol{r}_2 - \boldsymbol{r}_1$. At fixed $\boldsymbol{\Delta}$, we obtain a travel-time map by varying the central position $\boldsymbol{r}$. Throughout this paper, we only consider pairs of points for a fixed value of the separation distance, $\Delta = 9.9$ Mm. We use the simplifying assumption (Gizon & Birch 2002) that the sensitivity of *f*-mode travel times is restricted to a horizontal plane, which we call the "surface." As a result, we write the travel-time perturbation $\delta\tau(\boldsymbol{r}; \boldsymbol{\Delta})$ due a small-amplitude inhomogeneity on the surface, δq, as the two-dimensional (2D) spatial convolution of a kernel function, K, with δq:

$$\delta\tau(\boldsymbol{r}; \boldsymbol{\Delta}) = \int\int d\boldsymbol{r}'\, K(\boldsymbol{r}' - \boldsymbol{r}; \boldsymbol{\Delta})\delta q(\boldsymbol{r}'). \quad (1)$$

The inhomogeneity δq (e.g., a perturbation in temperature, density, etc.) is distributed over the whole surface. The integral is taken over all surface locations $\boldsymbol{r}'$. We only examine the mean travel time, i.e., the average $[\delta\tau(\boldsymbol{r}; \boldsymbol{\Delta}) + \delta\tau(\boldsymbol{r}; -\boldsymbol{\Delta})]/2$. In this scenario, the two-dimensional kernel function is calculated from theory. There are different kernel functions for different types of inhomogeneities, e.g., temperature, flow, density, magnetic field, damping, and source kernels, although these are not all independent (and have not all been calculated). As shown first by Woodard (1997), different perturbations may have similar effects on the travel times; in particular a damping perturbation may be confused with a flow perturbation. The details of the kernels, however, are specific to a particular type of perturbation. Thus, it would be useful to have additional measurements that could help us isolate which inhomogeneities are dominant. In the present paper, the quiet-Sun magnetic field is used as the perturbation. The magnetic field features are in general associated with

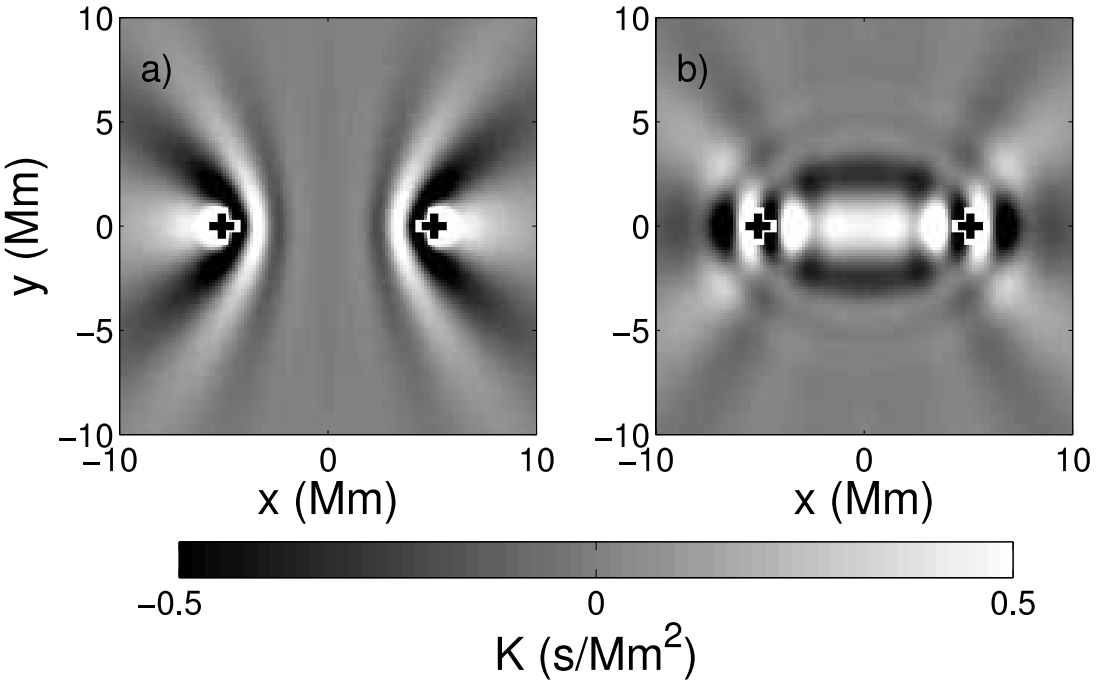

FIG. 1.—Theoretical kernels for mean travel time from Gizon & Birch (2002). (*a*) Kernel for source strength; (*b*) kernel for damping. The locations of the two observation points are indicated by the crosses.

the supergranulation network and have a lifetime long enough that travel times can be observed. They are reasonably isolated so that the fine structure of the kernel can be seen.

Examples of 2D *f*-mode theoretical kernels are shown in Figure 1 (Gizon & Birch 2002). The largest features are located near the two measurement points. In addition, other possibly observable features are present, including ellipses and hyperbolae whose foci are at the measurement points $\boldsymbol{r}_1$ and $\boldsymbol{r}_2$. We note that the elliptical features, which are due to scattering in a plane, are also seen in the 2D travel-time kernels studied in geoseismology (Tong et al. 1998). Hyperbolae result from the scattering of waves generated from distant source locations. Most features present in the picture are at the scale of the dominant wavelength of the waves analyzed, in this case 5 Mm. One might ask why we consider that damping might be an important process in small magnetic elements. It is not just classical damping (Murawski & Roberts 1993) that is important, but any conversion of *f*-mode energy into other waves, such as *p*-modes or MHD waves, would look like damping in a purely *f*-mode analysis. That such conversion processes might be important has been calculated in detail by Bogdan et al. (1996).

This paper is an attempt to measure a kernel function in equation (1). For the horizontal wavenumbers dominant in the Sun, about $l = 100$–1000, the surface gravity waves are horizontally propagating and confined to a thin layer (2 Mm) near the photosphere. This means that only a two-dimensional kernel need be considered, namely, the two horizontal spatial coordinates.

How would one of these 2D kernel functions be measured? Two methods have been developed and are presented here. In the first method small (smaller than a wavelength) inhomogeneities are found that are isolated and live long enough, a few hours, to measure travel-time variations in their neighborhood. Mathematically, if a spatial Dirac delta function is inserted into equation (1), then the kernel function is given directly by the travel-time map (feature method). If it is assumed that the perturbation, δq, in equation (1) is given by the observed magnetogram, a deconvolution can be performed to obtain the kernel from the observed travel times (deconvolution method).

In practice we were not able to find enough strong, isolated features to approximate a delta function. The resulting feature kernel is a smoothed version of the real kernel for magnetic features. However, it does show the important quantities of a kernel: strong features near the observation points, ellipses, and hyperbolae. This comes out of a very simple analysis, just averaging travel-time maps around features.

2. OBSERVATIONS AND ANALYSIS

Data from the high-resolution observing mode of the Michelson Doppler Imager (MDI) instrument (Scherrer et al. 1995) on the *Solar and Heliospheric Observatory* (*SOHO*) satellite have been used in this study. During 1996–1997 there was considerable observing time devoted to the study of the quiet Sun in this mode. The high-resolution mode of MDI has a 0.4 Mm sampling interval at disk center. As it may be difficult to resolve some of the smallest features in the kernels, it was decided to only use data with the full resolution. In general three variables were observed: line-of-sight velocity, line-of-sight magnetic field, and continuum intensity. For the present study, only the velocity and magnetic field have been analyzed. To obtain these three variables, telemetry limitations only permit a region of about 1024×500 pixels to be observed every minute. We studied 102 different 4 hr time periods, essentially all the data available during 1996–1997 with the full resolution and characterized in the catalog as "quiet Sun."

Both the velocity and magnetic field data have been projected onto Postel's azimuthal equidistant projection (Pearson 1990) and tracked using the small magnetic feature rotation rate (Komm et al. 1993). The tracked data include a combination of rectangular images (elongated in the east-west or north-south direction) and square images.

The velocity data cube is filtered to isolate the surface gravity waves, or *f*-modes. This is done by multiplying the three-dimensional Fourier transform of the data cube by a filter function.

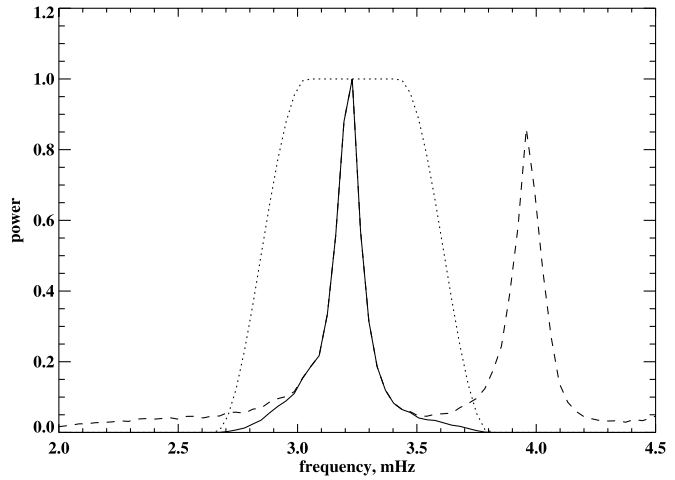

FIG. 2.—Filter (*dotted line*), unfiltered spectrum (*dashed line*), and filtered spectrum (*solid line*) at spherical harmonic degree $l = 1047$. The spectra have been normalized to unity at the peak. The peak near 3.2 mHz is the *f*-mode and that near 3.9 mHz is the p_1-mode. The filter has a flat part and a cosine bell part. The width of both parts is a function of the frequency separation of the *f*- and p_1-modes, $\Delta\nu(l)$, a function of the degree *l*. The published frequencies of Bachmann et al. (1995) were used. The full width of the flat part of the filter is $\Delta\nu/2$, and the cosine bell falls from 1 to 0 also in $\Delta\nu/2$.

The filter function and a filtered and unfiltered spectrum are shown in Figure 2.

The quiet-Sun magnetograms are significantly affected by cosmic-ray hits to the detector. These cause artifacts in the magnetograms that can be single or multiple pixels but in general are only present in a single minute's magnetogram. To remove these artifacts, the signal for a given spatial pixel is replaced by the median for 7 minutes in the tracked data. To characterize the perturbation function, the average magnetogram for 4 hr is computed and absolute value taken. The reason for computing this average is to get the properties of the magnetic field covering the same time period as the oscillation measurements. The absolute value of the magnetic field is taken, as we do not expect the perturbation to depend of the field polarity.

2.1. *Feature Method*

The features are defined by the following algorithm. From the 4 hr average magnetogram image, the location of the largest signal is used as the input guess position to a 2D Gaussian fit over a region 17×17 Mm. In addition to the normal Gaussian parameters, a constant background is added to characterize the magnetogram noise. The resulting fit parameters are stored in a table, and a 4×4 Mm region surrounding the feature center is zeroed in the image. This procedure is repeated to find the 100 largest features. The parameters for these 100 features are examined to consider which are suitable for the present study. Features with FWHM greater than 4 Mm are excluded as are pairs with separations less than 8 Mm. In addition, features closer than half of the size of the desired kernel from the edge of the image are also excluded. On average 25 magnetic features out of the original 100 remain for further study.

An overall average magnetic feature is derived from the average magnetic field surrounding each of the feature locations. This average feature for each 4 hr interval is then averaged over the 102 4 hr intervals. This overall average feature is then fit by a 2D Gaussian function plus background. The resulting parameters are peak field =76 G, FWHM = 2.6 Mm, and background =3.4 G. This puts the full width of the average feature at about half of the wavelength of the *f*-mode waves.

We analyzed the cross-correlations for a particular pair separation of 9.9 Mm, or 24 pixels in the Postels projection images. This particular separation was chosen as the smallest in which the envelope of the cross-correlation is completely separated from zero lag. In addition, this separation was chosen to make the comparison easier with the theory (Gizon & Birch 2002). The cross-correlations are computed in frequency space according to

$$\tilde{C}(x + \delta x/2, y + \delta y/2, \omega) = \tilde{v}^*(x, y, \omega)\tilde{v}(x + \delta x, y + \delta y, \omega), \quad (2)$$

where $\boldsymbol{r} = (x, y)$ is the location from equation (1), δx and δy are the shifts in x and y, $\tilde{C}(x + \delta x/2, y + \delta y/2, \omega)$ is the temporal Fourier transform of the cross-correlation at the horizontal coordinate (x, y), $\tilde{v}(x, y, \omega)$ is the temporal Fourier transform of the filtered velocity signal, and ω is the temporal frequency. It is important to characterize the location associated with the cross-correlation as below the location is compared to that of a feature. There are 73 combinations of δx, δy for which

$$23.5 \text{ pixels} \leq \sqrt{\delta x^2 + \delta y^2} \leq 24.5 \text{ pixels}, \quad (3)$$

which were used in the present study. The resulting two-point kernel needs to be derotated by the angle $\theta = \arctan(\delta y/\delta x)$.

For each of the 102 4 hr intervals and for each of the 73 angles θ, cross-correlations $C(x, y, \tau)$ were computed for the time lags -40 minutes $\leq \tau \leq 40$ minutes. Travel times were computed from these cross-correlations using the procedure described by Gizon & Birch (2004). This travel-time computation has the advantage of overcoming the limitation on noise level caused by the period of the waves and thus of making possible the measurement of the travel time between two individual points without additional spatial averaging. And in fact, the noise level for one-direction travel time for a single pair of pixels for the 4 hr interval is 2.5 minutes out of a travel time of 22 minutes.

These travel-time images are contaminated by a low spatial frequency variation of the time that varies approximately with the heliocentric angle. The range of variation over the images is about 1 s. Each travel-time image is fitted by least squares with a parabolic function, and the residuals to this fit are used for the later analysis. A center-to-limb variation of the mean travel time was noticed in a *p*-mode study by Duvall (2003). It may be that this type of problem is caused by applying the filter in the spatial Fourier domain. In future work it may be useful to apply filtering using spherical harmonics, as was done by Kholikov (2004). There is a small oscillation amplitude reduction in the magnetic features. It was pointed out by Rajaguru et al. (2006) that this can cause travel-time errors, when coupled with spacetime filters. A test was performed in which an amplitude correction was applied before filtering. The resulting kernels were different by less than 1 s from those presented below. In future work it will be useful to apply this amplitude correction routinely.

The kernel for the feature method is derived by averaging the travel times near 2475 magnetic features. To get the right units and magnitude for the kernel, the average travel-time map is divided by the average magnetic flux in a feature, 0.6 kG Mm^2. Figure 3*a* shows the feature-method kernel. Errors for this kernel are derived from the scatter of the 73 different orientations.

2.2. *Deconvolution Method*

The deconvolution method of measuring the kernel is conceptually more difficult but yields both higher resolution and

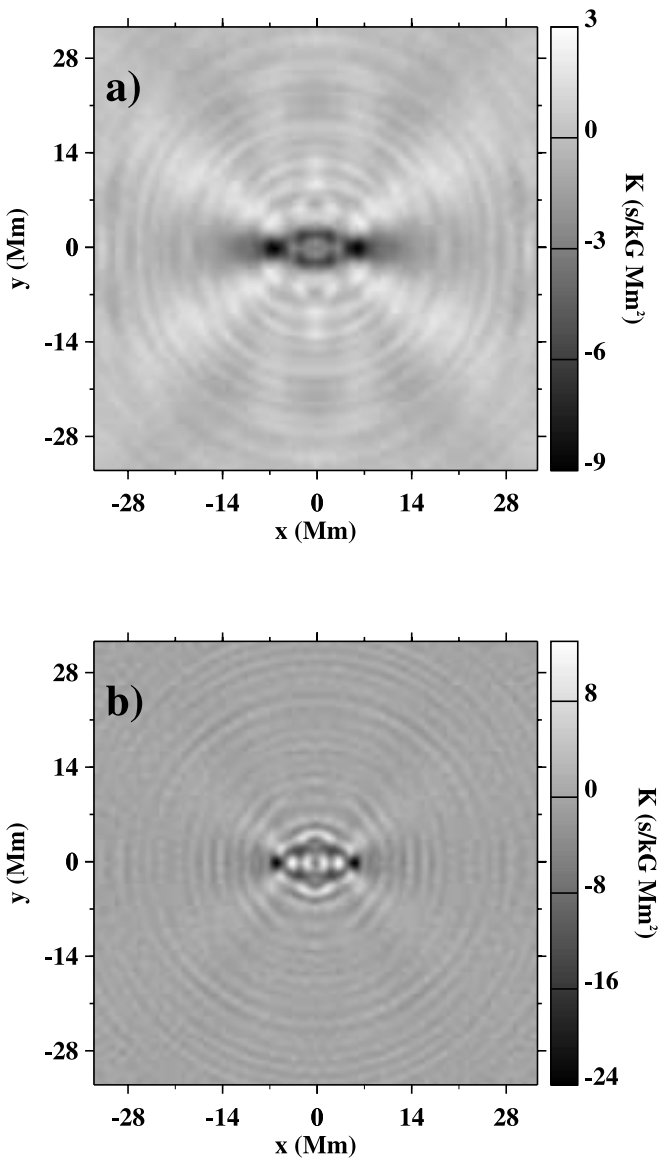

FIG. 3.—Observed kernels by (*a*) the averaged magnetic feature method; and (*b*) the relatively unfiltered deconvolution method. The coordinates of the two observation points are ($x = -5$ Mm, $y = 0$) and ($x = 5$ Mm, $y = 0$).

better signal-to-noise ratio, as all of the data are being used in an optimum way. If it is assumed that the perturbation in equation (1) is given by the absolute value of the line-of-sight magnetic field, then the observed travel-time map is given by the desired kernel convolved with the observed magnetogram. Taking the two-dimensional spatial Fourier transform and making use of the convolution theorem, a simple relation between the observables is obtained:

$$\tilde{O}(k_x, k_y) = \tilde{A}(k_x, k_y)\tilde{B}(k_x, k_y), \tag{4}$$

where $\tilde{O}$ is the Fourier transform of the observed travel-time map, $\tilde{A}$ is the Fourier transform of the kernel, $\tilde{B}$ is the Fourier transform of the magnetogram, and k_x, k_y are the components of the horizontal wavevector $\boldsymbol{k}$.

For each of the 73 orientations θ, the travel-time image is rotated so that the kernel is always aligned in the x-direction. The magnetogram is similarly rotated. Therefore, for each of the 73 orientations and 102 time intervals, the values of $\tilde{A}$ are constant

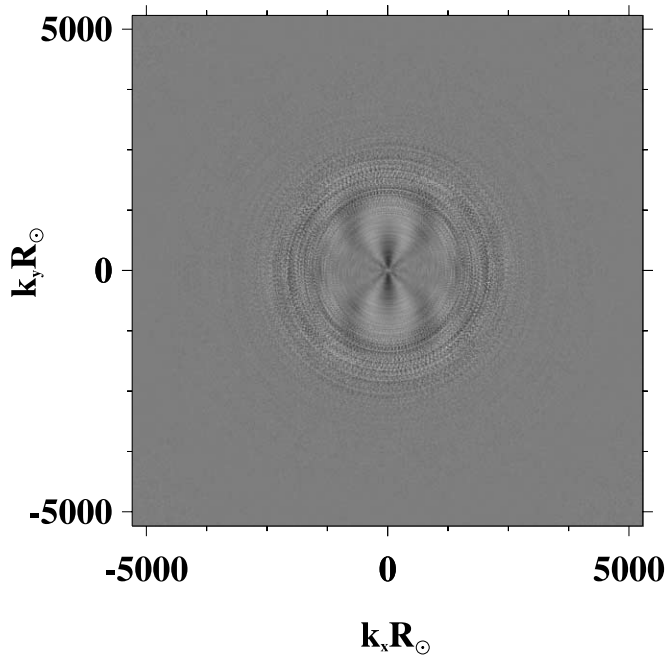

FIG. 4.—Real part of the spatial Fourier transform of the kernel. The wavenumbers k_x, k_y have been multiplied by the solar radius to give the number of waves in the circumference of the Sun. The transform coefficients become noisy for $kR_\odot > 1000$.

while the magnetic transform values $\tilde{B}$ cover a wide range of values. At each value of $\boldsymbol{k}$, a linear least-squares problem is solved to obtain the real and imaginary parts of $\tilde{A}$ and the errors. To obtain the errors, it was assumed that the scatter of the values of $\tilde{O}$ at a given $\boldsymbol{k}$ is due to random Gaussian noise, which seems reasonable. That this procedure actually works is shown by examining the real part of the derived coefficients of $\tilde{A}$ in Figure 4. The smooth lobes visible for $kR_\odot < 1000$ have a reasonable signal-to-noise ratio, as seen in Figure 5, where we have plotted the square root of the ratio of the azimuthally averaged mean-squared signal to that of the error. There seems to be no useful information in the imaginary part of the transform, so it is not used.

We present two versions of the kernel derived from these transform coefficients. An optimal version will be derived in a

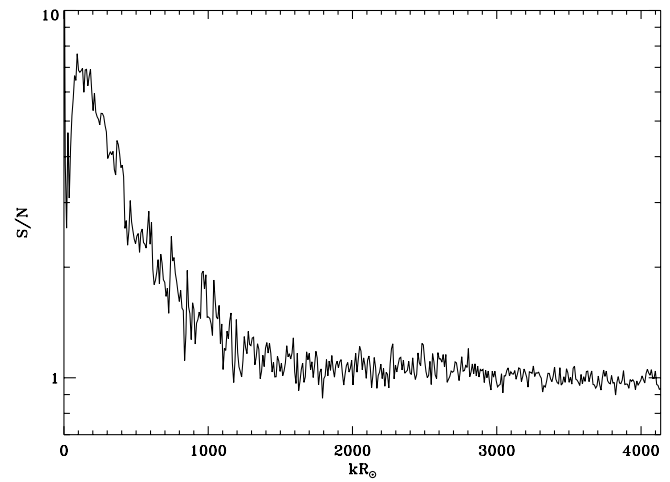

FIG. 5.—Estimate of the signal-to-noise ratio in the spatial Fourier domain, computed as the square root of the ratio of the azimuthally averaged mean-squared signal to the azimuthally averaged mean-squared error.

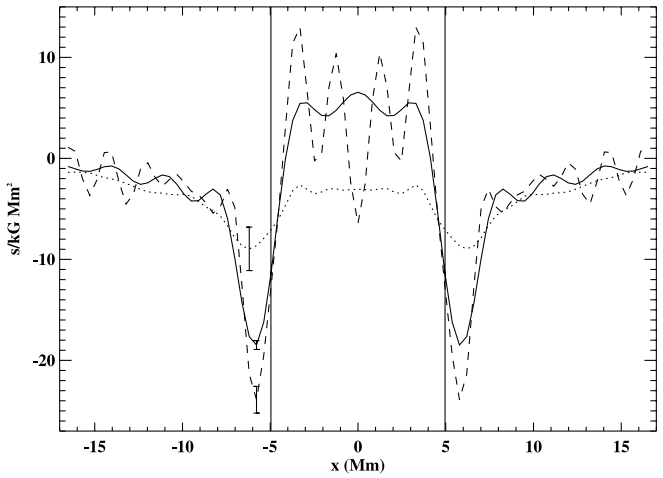

FIG. 6.—Cut through the observed kernels in the x-direction at $y = 0$. The solid curve is the more strongly filtered deconvolution kernel, and the dashed curve is the relatively unfiltered deconvolution kernel. The dotted curve is the feature kernel. Characteristic 5 σ errors are shown near the minima at $x = -6$ Mm. The vertical lines near $x = \pm 5$ Mm denote the locations of the two observation points.

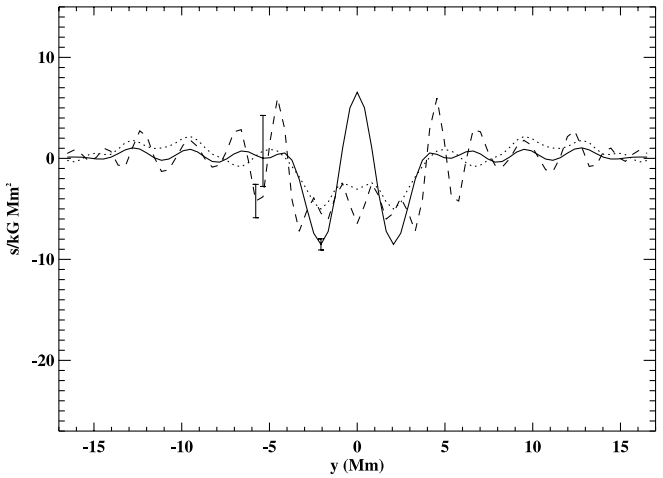

FIG. 7.—Cut through the observed kernels in the y-direction at $x = 0$. The solid curve is the more strongly filtered deconvolution kernel, and the dashed curve is the relatively unfiltered deconvolution kernel. The dotted curve is the feature kernel. Characteristic 5 σ errors are shown leftward of the center.

future paper. In the first, relatively unfiltered version, the coefficients with $kR_\odot > 2750$ are zeroed before the inverse Fourier transform is computed. This version is shown in Figure 3*b*. The units were obtained by dividing by the area of an individual pixel, $(0.41\ \mathrm{Mm})^2$. Errors have been determined by using the errors of the transform values in a Monte Carlo calculation to get errors in the x-y domain. The second version of the kernel is derived by filtering the transform coefficients based on the signal-to-noise ratio in Figure 5. A smooth truncation of the transform is done centered at $kR_\odot = 1380$, the location where the signal-to-noise ratio falls to approximately 1. The truncation goes from 1 to 0 over a range of $kR_\odot = 260$. This filtered version of the kernel is compared with the model (derived in § 3) in Figure 8.

The deconvolution kernel has more resolution than the feature-averaged one, as one might expect. A comparison of the two versions of the deconvolution kernel with the feature kernel at $y = 0$ is shown in Figure 6. The peak signal-to-noise ratios of the kernels are 168 for the filtered deconvolution kernel, 72 for the unfiltered deconvolution kernel, and 27 for the feature kernel.

The elliptical features present in the theoretical damping kernel (Fig. 1*b*) are also present in the measured kernel. These features are due to scattering (Gizon & Birch 2002). This suggests that the observed kernel is not dominated by the effect of local changes in wave sources (Fig. 1*a*), which do not cause these features. The elliptical features are better seen in a cut through the image at $x = 0$ in Figure 7.

3. A SIMPLE MODEL

In this section we develop a simple phenomenological model to explain the basic features of the travel-time observations. We assume that scattering from a small magnetic element can be described as a combination of monopole and dipole scattering. This assumption is motivated by studies of the interaction of waves with slender magnetic tubes (e.g., Bogdan et al. 1996) that show that these two modes are dominant. We then adjust the amplitudes and phases of these two types of scattering in order to obtain a model that reproduces the observations.

We begin from the simple *f*-mode example described in detail in Gizon & Birch (2002). This study provides a method to compute the first-order travel-time perturbation due to scattering in the horizontal plane, given an expression for the perturbation to the wave operator, $\delta\mathcal{L}$ (we keep the notations of Gizon & Birch 2002). Here we choose very simple phenomenological models for the monopole and dipole scattering operators acting on an incoming wave packet (velocity $\boldsymbol{v}$). For the case of monopole scattering we introduce the operator $\delta\mathcal{L}_{\mathrm{mono}}$, which we define as

$$\delta\mathcal{L}_{\mathrm{mono}}\boldsymbol{v} = m(\boldsymbol{r})e^{i\phi_{\mathrm{mono}}}kw. \tag{5}$$

In the above equation, k is the horizontal wavenumber, $\boldsymbol{v}$ is the wave velocity, and w is the vertical component of $\boldsymbol{v}$. The function $m(\boldsymbol{r})$ gives the local strength of the monopole scattering and ϕ_{mono} the phase of the scattering, which we assume is independent of position. For the case of dipole scattering we use

$$\delta\mathcal{L}_{\mathrm{dip}}\boldsymbol{v} = \nabla_h \cdot \left[d(\boldsymbol{r})e^{i\phi_{\mathrm{dip}}}\boldsymbol{v}_h\right]. \tag{6}$$

In the above equation the subscript h denotes the horizontal part. The function $d(\boldsymbol{r})$ gives the local strength of the dipole scattering and ϕ_{dip} the phase. The phases ϕ_{mono} and ϕ_{dip} allow us the freedom to adjust the phases of the monopole and dipole scattered waves. Using the model of Gizon & Birch (2002) we can obtain the first-order sensitivity of the *f*-mode travel times to the functions $m(\boldsymbol{r})$ and $d(\boldsymbol{r})$. These linear sensitivity kernels, K_m and K_d, to the *f*-mode mean travel times satisfy

$$\delta\tau_{\mathrm{mean}}(\boldsymbol{r};\boldsymbol{\Delta}) = \int\int d\boldsymbol{r}'\, K_m(\boldsymbol{r}'-\boldsymbol{r};\boldsymbol{\Delta})m(\boldsymbol{r}') + \int\int d\boldsymbol{r}'\, K_d(\boldsymbol{r}'-\boldsymbol{r};\boldsymbol{\Delta})d(\boldsymbol{r}'). \tag{7}$$

The variables $\boldsymbol{r}$, $\boldsymbol{r}'$, and $\boldsymbol{\Delta}$ are the same as in equation (1).

By comparing the predictions of the simple phenomenological model described in the previous paragraph with the observed travel times, we can estimate the free parameters in the model. We write the model kernel at fixed $\boldsymbol{\Delta}$ as

$$K_{\mathrm{model}}\left(\boldsymbol{r};\beta,\phi_{\mathrm{mono}},\phi_{\mathrm{dip}}\right) = A[K_m(\boldsymbol{r}) + \beta K_d(\boldsymbol{r})]. \tag{8}$$

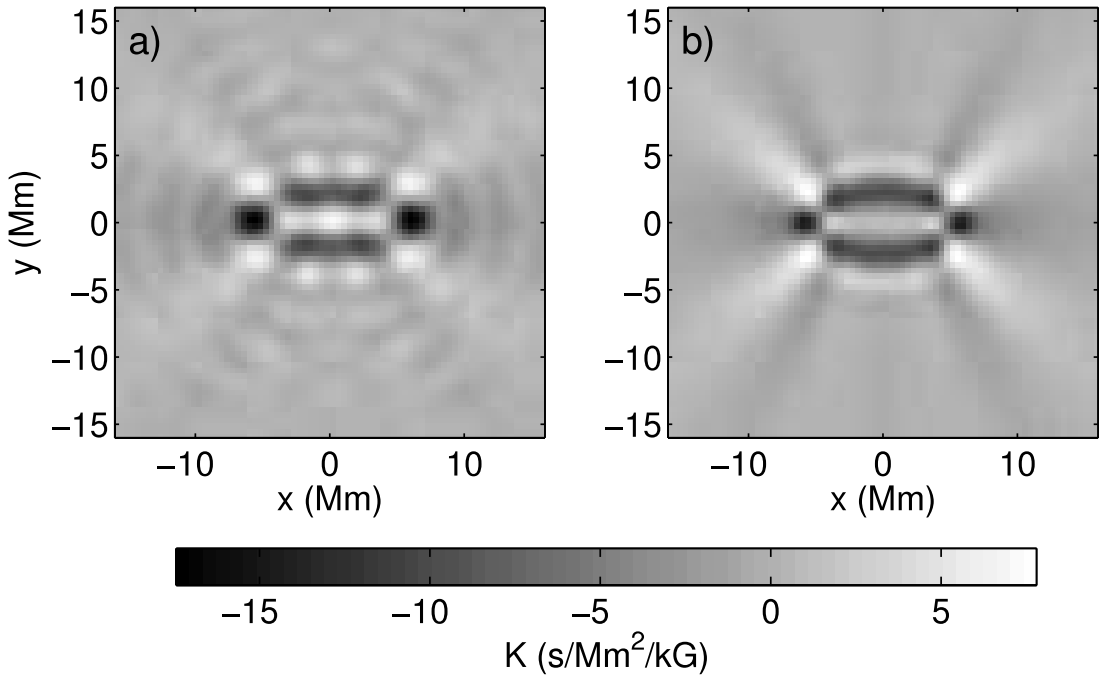

FIG. 8.—Comparison of (*a*) the more strongly filtered deconvolution kernel with (*b*) the model kernel. The kernels are plotted using the same gray scale. The model reproduces many of the features of the measured kernels; in particular the ellipse- and hyperbola-shaped features appear in roughly the same places with the same amplitudes. Note that the observed kernel contains more detailed structure along the line $y = 0$ than the model.

Note that K_m depends on $\phi_{\rm mono}$ and K_d depends on the $\phi_{\rm dip}$. The ratio between the dipole and monopole contributions is given by β. For each value of β and the phases we fix the amplitude A by demanding that the rms, over $\boldsymbol{r}$, of the model and the data are the same. We then determine β, $\phi_{\rm mono}$, and $\phi_{\rm dip}$ by doing a least-squares fit to the data; i.e., we minimize the difference between the observed kernel, $K_{\rm data}$, and the model kernel

$$X\left(\beta, \phi_{\rm mono}, \phi_{\rm dip}\right) = \sum\nolimits_{\boldsymbol{r}} \left[K_{\rm model}\left(\boldsymbol{r}; \beta, \phi_{\rm mono}, \phi_{\rm dip}\right) - K_{\rm data}(\boldsymbol{r})\right]^2 \tag{9}$$

over the three free parameters: β, $\phi_{\rm mono}$, and $\phi_{\rm dip}$. The fitted value of $\beta = 0.9$ together with the value of A obtained by matching the overall amplitude of the observed kernel imply an amplitude of d that is 1.5×10^{-4} s^{-2} Mm^{-2} kG^{-1} and an amplitude of m that is 1.4×10^{-4} s^{-2} Mm^{-2} kG^{-1}.

Figure 8 shows a comparison between the model described in the previous paragraph and the observed kernel. The model reproduces the main features of the observed kernel. The ellipse- and hyperbola-shaped features are of roughly the same amplitude and in the same locations. The observed kernel has some fine structure along the line $y = 0$ that is not reproduced by the model. This may indicate that in the model the bandwidth of the scattered wave is too large.

4. CONCLUSIONS AND FUTURE WORK

The kernel for small magnetic features to make travel-time variations has been measured by two techniques. The deconvolution technique is superior to the average-feature technique as it gives better resolution and peak signal-to-noise ratio. A simple model has been presented for the scattering from small magnetic elements that is similar to the observed kernel. It is likely that more detailed modeling will yield valuable information about the structure of magnetic features in the solar atmosphere.

This paper presents the first observational evidence to suggest that it is appropriate to use the Born approximation to compute kernels (as opposed to the ray approximation). The observed hyperbolic features confirm that it is important to take into account scattering of the waves coming from distant source locations (as opposed to the single-source approximation; Gizon & Birch 2002).

There are a number of potential extensions to the present work. *P*-modes can be used in addition to *f*-modes. The *p*-modes will have kernels that are three-dimensional structures of which we could only measure the surface component. This may be enough to give information about the structure of the "point" scatterers that are chosen. The time difference can be measured in addition to the mean travel time. Other surface perturbations can be used, for example, the granulation. The scattering from granulation can be studied from the present data using the observed intensity signal. It may be possible to measure the kernels for mode mixing by cross-correlating the *f*-mode signals with those for the p_1 ridge.

The MDI project is supported by NASA contract NAG5-13261 to Stanford University. *SOHO* is a project of international cooperation between ESA and NASA. The work of A. C. B. was supported by NASA contract NNH04CC05C. We wish to thank P. Milford for useful comments on the manuscript.

REFERENCES

Bachmann, K. T., Duvall, T. L., Jr., Harvey, J. W., & Hill, F. 1995, ApJ, 443, 837
Birch, A. C., Duvall, T. L., Jr., & Kosovichev, A. G. 2004, ApJ, 608, 580
Birch, A. C., & Kosovichev, A. G. 2000, Sol. Phys., 192, 193
Bogdan, T. J. 1997, ApJ, 477, 475
Bogdan, T. J., Hindman, B. W., Cally, P. S., & Charbonneau, P. 1996, ApJ, 465, 406
D'Silva, S., & Duvall, T. L., Jr. 1995, ApJ, 438, 454
Duvall, T. L., Jr. 2003, in Proc. *SOHO* 12/GONG+ 2002 Workshop, ed. H. Sawaya-Lacoste (ESA SP-517; Noordwijk: ESA), 259
Duvall, T. L., Jr., Jefferies, S. M., Harvey, J. W., & Pomerantz, M. A. 1993, Nature, 362, 430
Gizon, L., & Birch, A. C. 2002, ApJ, 571, 966
———. 2004, ApJ, 614, 472
Kholikov, S. 2004, in Proc. *SOHO* 14/GONG 2004 Workshop, ed. D. Danesy (ESA SP-559; Noordwijk: ESA), 513
Komm, R. W., Howard, R. F., & Harvey, J. W. 1993, Sol. Phys., 145, 1
Kosovichev, A. G. 1996, ApJ, 461, L55
Murawski, K., & Roberts, B. 1993, A&A, 272, 595
Pearson, F. 1990, Map Projections: Theory and Applications (Boca Raton: CRC)
Rajaguru, S. P., Birch, A. C., Duvall, T. L., Jr., Thompson, M. J., & Zhao, J. 2006, ApJ, in press
Scherrer, P. H., et al. 1995, Sol. Phys., 162, 129
Tong, J., Dahlen, F. A., Nolet, G., & Marquering, H. 1998, Geophys. Res. Lett., 25, 1983
Woodard, M. F. 1997, ApJ, 485, 890